

# Blob birth and transport in the tokamak edge plasma: analysis of imaging data

J. R. Myra, D. A. D'Ippolito

*Lodestar Research Corp., 2400 Central Ave. P-5, Boulder, Colorado 80301*

D. P. Stotler, S. J. Zweben, B. P. LeBlanc, J.E. Menard

*Princeton Plasma Physics Laboratory, Princeton, New Jersey 08540*

R. J. Maqueda

*Nova Photonics, Princeton, New Jersey 08540*

J. Boedo

*University of California at San Diego, La Jolla, California 92093*

June 2006 (revised August 2006)

submitted to Phys. Plasmas

---

DOE/ER/54678-1

LRC-06-110

---

**LODESTAR RESEARCH CORPORATION**

*2400 Central Avenue  
Boulder, Colorado 80301*

## Abstract

High-speed high-spatial-resolution data obtained by the gas puff imaging (GPI) diagnostic on the National Spherical Torus Experiment (NSTX) [M. Ono, M.G. Bell, R.E. Bell *et al.*, Plasma Phys. Control. Fusion **45**, A335 (2003)] is analyzed and interpreted in light of recent theoretical models for edge turbulence and blob propagation. The experiment is described in terms of theoretical regimes which predict different dependencies for the radial velocity of blob convection. Using the GPI data, atomic physics analysis, and blob tracking on a restricted dataset, it is shown that the observed blob velocities in the scrape-off-layer are bounded by a theory-based minimum velocity associated with the sheath-connected regime. A similar maximum velocity bound associated with the resistive-ballooning regime is also observed. Turning to the question of blob creation, it is shown that blobs are born with a density and temperature characteristic of the plasma conditions where underlying linear edge drift-curvature instabilities are localized. Finally, statistical variations in blob properties and in the radial blob velocity for given edge conditions are significant, and tend to mask any systematic changes among discharges with different conditions.

PACS: 52.55.Fa, 52.70.Kz, 52.35.Ra, 52.25.Fi, 52.40.Hf

## I. Introduction

Edge turbulence, observed for decades on tokamaks and other magnetic confinement devices,<sup>1-3</sup> is of great contemporary importance in the field of fusion energy research. It is widely recognized that the edge plasma is critical for several reasons. Proper handling of the energy and particles exhausted by the core plasma is required to control damage to plasma facing components, wall content (e.g. tritium inventory) impurities and recycling in present and future high-performance devices. Understanding the turbulent scrape-off-layer (SOL) will likely be necessary to optimize the environment for rf antennae. Finally, the physics of edge instabilities, turbulence, strong nonlinearity, convective transport and the emergence of coherent structures is both interesting in its own right and of practical importance for first principles models and simulations of tokamak confinement.

Recent experimental observations of intermittent convective transport in the SOL plasma<sup>4-15</sup> (see also numerous contained references) have spawned a rapidly growing literature addressing the theory and simulation of these phenomena<sup>16-26</sup> and other related edge and pedestal turbulence issues<sup>27-29</sup> (such as zonal flows, turbulence regulation, magnetic and flow shear, transport barriers). Two conference review papers describe additional background on these topics.<sup>30,31</sup>

While numerical simulations are required to obtain detailed predictions of the strongly nonlinear edge and SOL turbulent dynamics, semi-analytic “blob” models<sup>16-20</sup> (describing the convective propagation of filamentary objects) have been proposed to provide physical insight, and to guide the interpretation of both experiments and simulations. Theoretical work has established the existence of several regimes of blob propagation.<sup>32,33</sup> These regimes show different dependencies for the radial convection velocity of blobs on plasma and machine parameters.

Modern two-dimensional high-speed, high-spatial resolution imaging techniques<sup>14,15,34</sup> provide an opportunity to compare some of theoretical concepts and blob velocity scalings against experimental results. This is the main goal of the present paper. Many experimental papers have measured the blob radial convection velocity,  $v_r$ . Typical results are in the range of a few hundred to a thousand or so m/s corresponding to 1-10% of the local sound speed in the SOL. Similarly, many theoretical and simulation papers have shown that speeds in this range are roughly consistent with blob models. In this paper we go one step further and present a detailed analysis of experimental data from the National Spherical Torus Experiment<sup>35</sup> (NSTX) for  $v_r$ , its correlation with blob parameters, and with corresponding quantitative theoretical scaling predictions.

The penetration of plasma into the SOL and its impact on material surfaces is controlled by the competition between radial convection and classical parallel flow to limiters and divertor plates. Thus, our goal of understanding  $v_r$  and its dependence on plasma and machine parameters is one important ingredient of a complete picture of plasma in the SOL. We will also address the question of what plasma properties blobs are born with. Ultimately, a description of the particle and heat fluxes will also require a characterization of the rate of blob generation, a topic which is mostly outside the scope of the present study.

The plan of our paper is as follows. In Sec. II we review some theory background motivating the present study, and characterize the various blob regimes. Section III briefly summarizes the experiments and the analysis procedure employed here, while the results of the analysis are given in Sec. IV. Finally, Sec. V contains further discussion and conclusions.

## II. Theory background and blob regimes

Blobs, described in detail elsewhere,<sup>16,20</sup> can be thought of as flux tubes in the SOL which contain (much) more plasma than their surroundings. These coherent propagating objects, created from edge turbulence, are filamentary along the magnetic field  $B$ , and typically have cm-like scale lengths across  $B$ . The charge separation resulting from curvature and grad- $B$  drifts (typically dominated by ballooning effects at the outboard midplane) acts as a current source. Current flow along and across the field lines compete (via their effective resistances) to establish current loops and circuit paths. (See for example Fig. 1 of Ref. 32). Each current loop, or equivalent circuit, corresponds to both an edge instability and a blob propagation regime. These regimes, including the effect of X-point (divertor) geometry and electromagnetism, have been presented in detail previously for the “disconnected” regimes, where current to the sheaths is negligible.<sup>32</sup>

To understand the scaling of the blob convective velocity,  $v_r$ , in general, an electrostatic two-region model has recently been proposed. Details of this model will be presented elsewhere;<sup>36</sup> here we motivate the results necessary to characterize experimental results that will be of subsequent interest. The dimensionless parameters of the model describe collisionality through

$$\Lambda = \frac{v_{ei}L_{\parallel}}{\Omega_e \rho_s} = 1.7 \times 10^{-14} \frac{n_e L_{\parallel}}{T_e^2} \quad (1)$$

and blob scale size through

$$\hat{a} = \frac{a_b}{a_*} = \frac{a_b R^{1/5}}{L_{\parallel}^{2/5} \rho_s^{4/5}} = 0.018 \frac{a_b B^{4/5} R^{1/5}}{L_{\parallel}^{2/5} T_e^{2/5}} \quad (2)$$

where the final forms of these (and subsequent) equations express inputs in the units:  $n_e(\text{cm}^{-3})$ ,  $B(\text{G})$ ,  $L_{\parallel}(\text{cm})$ ,  $R(\text{cm})$ ,  $T_e(\text{eV})$ ,  $a_b(\text{cm})$  and we have assumed a deuterium plasma. Here  $v_{ei}$  is the Coulomb collision frequency,  $\Omega_j$  ( $j = i, e$ ) the species gyro-

frequency and  $\rho_s = c_s / \Omega_i$  the ion Larmor radius based on the electron temperature  $T_e$ .  $R$  is the tokamak major radius,  $L_{\parallel} = qR$  the parallel blob connection length, and  $a_b$  is the blob scale size (nominal blob radius). Note that the symbol  $q$  is *not* used in this paper to denote the tokamak safety factor, although it is related to the magnetic geometry, a point that is discussed further in Sec. IV.

In Eq. (2),  $a_b$  is normalized to a scale  $a_* = L_{\parallel}^{2/5} \rho_s^{4/5} / R^{1/5}$  that arises by competing cross-field ion polarization current with sheath end-loss current.<sup>19</sup> Generalizing earlier work, the present regime model also includes the physics of X-point-induced disconnection,<sup>26,37,38</sup> described by a geometrical “fanning” factor  $\varepsilon_x$  that is defined in detail in Ref. 32. For typical divertor flux geometry,  $\varepsilon_x$  is approximately linear with distance from the separatrix and  $\varepsilon_x \sim 0.1$  at a distance of 1 cm into the SOL. In the theory,  $\varepsilon_x$  influences the locations of the regime boundaries. (e.g. see Fig. 2 of Ref. 32)

The resulting regime diagram for blob propagation is shown in Fig. 1, which also indicates nominal locations of the NSTX and Alcator C-Mod<sup>39</sup> edge (near separatrix) plasmas. These disks correspond to the cases:  $n_e = 3 \times 10^{12} \text{ cm}^{-3}$ ,  $T_e = 20 \text{ eV}$ ,  $a_b = 2 \text{ cm}$ ,  $q = 3.5$ ,  $R = 150 \text{ cm}$ ,  $B = 2.5 \text{ kG}$  for NSTX, and  $n_e = 1 \times 10^{14} \text{ cm}^{-3}$ ,  $T_e = 25 \text{ eV}$ ,  $a_b = 0.5 \text{ cm}$ ,  $q = 3.5$ ,  $R = 88 \text{ cm}$ ,  $B = 40 \text{ kG}$  for Alcator C-Mod, with roughly factor-of-two variation in  $n_e$ ,  $T_e$  and  $a_b$ . In each of the regimes, resistive ballooning (RB), resistive X-point (RX), and sheath-connected interchange (C), the blob velocity  $v_r$  obeys a particular scaling with plasma and machine parameters.<sup>32</sup> In general,  $v_r$  increases in moving up and to the left in the diagram. A characteristic velocity based on theoretical considerations is given by

$$v_* = c_s \left( \frac{a_*}{R} \right)^{1/2} = 5.1 \times 10^6 \frac{L_{\parallel}^{1/5} T_e^{7/10}}{B^{2/5} R^{3/5}} \quad (3)$$

In terms of this characteristic velocity, the dimensionless ratio  $v_r/v_*$  is bounded from above and below:

$$\frac{1}{\hat{a}^2} < \frac{v_r}{v_*} < \hat{a}^{1/2} \quad (4)$$

where the lower bound physically represents the sheath-connected (C) limit with  $\hat{a} > 1$ , investigated in Refs. 16, 17 and the upper bound arises in the resistive (RB) limit discussed in Refs. 19, 26 and recently in Ref. 40 (where the blob velocity scaling in the RB limit is referred to as inertial scaling).

The minimum blob velocity occurs in the sheath-connected limit because in this case current is free to flow along the field lines and is regulated only by the sheath boundary condition. This situation provides the minimum circuit resistance, hence the minimum blob (dipole) potential and  $E \times B$  speed for a given curvature drive (which provides a constant current source). In the opposite limit of high collisionality (RB regime), parallel resistance impedes current flow to the sheaths, and instead the current loops are forced to close by ion polarization current across field lines. In this circumstance the circuit resistance, blob potential, and  $E \times B$  speed are large.

Thus, theoretically the blob speed  $v_r$  depends on  $a_b$ ,  $n_e$ ,  $T_e$ , magnetic geometry (through  $L_{||}$  or  $q = L_{||}/R$ , and X-point magnetic shear through  $\epsilon_x$ ) and the machine parameters  $R$  and  $B$ . In addition simulation studies and heuristic arguments have shown that when blobs propagate on a background plasma (as opposed to freely propagating through a vacuum) their velocity is slowed by a factor of order

$$f_b \sim \frac{\delta p}{p} \quad (5)$$

where  $p$  is the total pressure at the center of the blob and  $\delta p = p - p_0$  where  $p_0$  is the background pressure.<sup>20</sup> A more precise definition of  $f_b$  is given in the Appendix.

Although NSTX and Alcator C-Mod explore very different regions of parameter space (relative  $B$  and  $n_e$  ratios are about 16 and 30 respectively), Fig. 1 shows that their dimensionless parameters are not so different. Experimentally the observed blob velocities for both machines are an order unity fraction of  $v_* \sim 2$  km/s, the characteristic theory-based velocity for both machines. This type of rough agreement on convective velocities between theory and experiment has been noted in much of the theory and simulation literature. The main new result of the present paper will be making detailed experimental contact with the bounds described by Eq. (4).

### III. Experiment and analysis procedure

Gas puff imaging (GPI) supplemented by Thomson scattering (TS) provides the data for the analysis presented here. The GPI diagnostic has been described in detail elsewhere.<sup>14,15,34</sup> The basic idea behind GPI is to puff a small amount of neutral gas, helium in these experiments, into the edge plasma and view the resulting visible light emission by a fast camera. The camera produces a time sequence of two-dimensional images (i.e. a “movie”) which shows the helium light emission. When viewed along the magnetic field lines, the emission pattern enables a visualization of the turbulence and blob dynamics normal to  $B$ . The intensity of light emission is a function of the local plasma density and temperature through atomic rate coefficients. Consequently, with a knowledge of the local neutral helium density and the atomic physics, information about the local plasma density and temperature fluctuations can be extracted. A zoomed-in portion of a sample GPI frame is shown in Fig. 2.

Several procedures for analyzing the GPI data were employed. The most sophisticated analysis had four main steps: (i) use of atomic and radiation physics to obtain plasma density and temperature from the measured GPI intensity, (ii) blob identification and selection, (iii) blob tracking and measurement of  $v_r$ , and (iv) blob

database analysis. Step (i) is considered subsequently; steps (ii) – (iv) are described in more detail in the next section. Basically, once the criteria for blob selection have been satisfied, their speeds can be measured from the GPI movies. In practice, this is done by tracking the frame-to-frame location of (smoothed) local maxima of the intensity pattern. The result of these steps is a database of blob parameters and velocities (at each time instant). Most results described in the next section were obtained using the full analysis (i) – (iv) applied to one shot. Additionally, a semi-automated and less laborious procedure using steps (ii) – (iv) was employed to compare some features of four separate discharges.

For these experiments a camera framing rate of 4  $\mu$ s was employed, for a total of 300 frames, and the camera resolution of  $64 \times 64$  pixels covered approximately 23 cm in the radial and poloidal directions. Most of the analysis which follows was performed on shot #112825 which was a low confinement mode (L-mode) discharge with  $B_0 = 4.5$  kG ( $B = 2.5$  kG at the outboard midplane location viewed by GPI), plasma current  $I_p = 800$  kA, neutral beam power  $P_{nbi} = 0.8$  MW. The GPI camera was fitted with an HeI filter at 587.6 nm to allow quantitative interpretation of the intensity in terms of plasma parameters as described next.

The He 587.6 nm line intensity is given by

$$I = n_0 F(n_e, T_e) \quad (6)$$

where  $n_0$  is the neutral ground state He density and the function  $F(n_e, T_e)$  is known from the single state collisional radiative model.<sup>41–43</sup> A measurement of  $I$  can be used to infer  $n_e$  and  $T_e$  provided that  $n_0$  can be determined and we have some means of relating  $n_e$  and  $T_e$ . First we discuss an empirical procedure for obtaining  $n_0$ .

The idea is to “calibrate”  $I$  against  $n_e$  and  $T_e$  under a “known” set of conditions by using Thomson scattering measurements of  $n_e$  and  $T_e$ , thus obtaining an effective  $n_0 \sim$

$I/F(n_e, T_e)$ . The available Thomson scattering measurements are one-dimensional (with varying radial coordinate). Thomson scattering captures an essentially instantaneous snapshot of the radial profiles, usually missing the intermittent blob activity. To construct a comparative situation from the GPI images, we use the *median over time* of the 300 frames in the GPI movies. (The median operation, unlike averaging, eliminates most of the intermittent activity.) Having obtained in this way the 2D spatial structure of  $n_0$  for a given shot at a time near the GPI movies, it is then assumed that  $n_0$  is constant on the time scale of the turbulence and blobs for all 300 GPI frames. To summarize,

$$n_0 = \frac{\langle I \rangle_{t, \text{median}}}{F(n_e, T_e)_{\text{TS, probe}}} \quad (7)$$

where the 1D radial measurements of  $n_e$  and  $T_e$  used for  $F$  are assumed to be spatial constants on the flux surface. Radial profiles of  $n_e$ ,  $T_e$  and the empirically inferred  $n_0$  are shown in Fig. 3.

An additional simplification may be made for the interchange and convective plasma motions that are postulated to describe edge turbulence and blob propagation. The basic physics of curvature driven instabilities is the interchange of plasma on one flux tube with another flux tube containing lower pressure. The interchange motion is mediated by  $\mathbf{E} \times \mathbf{B}$  drifts and convects the higher pressure plasma in the direction of  $-\nabla_{\perp} B$ . The same mechanism is the basis for both the familiar linear curvature-driven interchange instability and the radial convective motion of blobs.<sup>16,17</sup> This convective motion of bulk plasma passively carries *both* density and temperature,  $n_e$  and  $T_e$  with it. Thus on short time scales (before parallel particle and energy losses drain the field line, and blobs no longer exist) we can make the convective ansatz

$$T_e = T_e(n_e) \quad (8)$$

The convective ansatz, together with Eq. (6), and a knowledge of  $n_0$ , allows a unique mapping between the measured time and space-resolved turbulent intensity  $I(x, y; t)$  and the plasma (e.g. blob) properties  $n_e(x, y; t)$  and  $T_e(x, y; t)$ . Here  $x$  and  $y$  are local radial and poloidal Cartesian variables. We will refer to Eq. (8) as the weak form of the convective ansatz. As one proceeds into the SOL the value of  $n_0$  deduced from Eq. (7) becomes singular (i.e. error prone) because, with the intermittent blobs removed, both numerator and denominator become small. To circumvent this problem we invoke a stronger form of the convective ansatz; namely, that on short time scales blobs propagate their density and temperature radially without modification. We will apply this convective ansatz in its weak form near the birth zone, and in its strong form deeper into the SOL, in all the analyses presented here that require information on the blob plasma parameters.

Finally, with regard to the atomic physics analysis described in the preceding paragraphs, we note that there is a nonlinear relationship between the raw camera signal and the emission incident on it. A nonlinear camera calibration was applied to the data to determine the intensity  $I$  from the raw signal, before applying Eqs. (6) and (7). For present purposes, an absolute calibration (including multiplicative constant) is not necessary.

Similar results to those presented in this paper were obtained using DEGAS-2 modeling for a first principles calculation of  $n_0$ , although this approach is more challenging, even for simulating the time-median situation.<sup>43</sup>

## IV. Results

In this section, we first present an analysis of blob behavior for NTSX shot #112825, illustrating in Figs. 4 – 7 experimental confirmation of the theoretical bounds for  $v_r$ . The location of the blob birth zone is also investigated (Fig. 8). In the remainder

of this section we undertake a less detailed analysis (Figs. 9 – 11) of a few more shots under varying discharge conditions. This analysis compares systematic variations between shots with intrinsic turbulence-induced variations for a single shot.

The difficulty of deducing blob velocity scalings directly from “raw” data is illustrated in Fig. 4 which shows the observed radial velocity of a few blob tracks vs. radial distance from a nominal separatrix location. (In this paper, the quoted separatrix location was determined by an equilibrium reconstruction which includes constraints from magnetics measurements, and requires the edge  $T_e$  from Thomson scattering to be constant on a flux surface, from the low-R side to the high-R side.) Colors (shades) in Figs. 4 – 7 are consistent, i.e. denote the same blob tracks; however, identification of individual blob tracks is not necessary for any of the points made in the following discussion. The particular blob tracks shown in the figure were selected from the GPI movie for this shot, based on several subjective criteria: brightness, image quality, symmetry, coherence, longevity, and isolation from the frame edges and from other blobs. These criterion are meant to improve the possibility for making contact with analytical  $v_r$  scalings which assume coherent, isolated, symmetric structures. Two features are immediately evident: (i) there is a large variation in  $v_r$  among the different blobs, (ii) both acceleration and deceleration can be seen for given blobs as they propagate outwards. There is little apparent order in this dataset, underscoring the need for a theoretical framework. These same blob tracks, subject to different analyses, are the dataset for the next three figures.

From Fig. 1, we expect that the data should lie marginally in the sheath-connected regime. This regime obeys the blob velocity scaling<sup>16,17,32</sup>

$$v_{r,C} = qc_s f_b \frac{\rho_s^2}{a_b^2} \sim 1.4 \times 10^{10} \frac{f_b q T_e^{3/2}}{a_b^2 B^2} \quad (9)$$

where  $q = q(r)$  as a result of the magnetic geometry. Recall that  $q = L_{\parallel}/R$  is not the safety factor, but rather the ratio of a blob parallel scale length to the tokamak major radius. For a uniform pressure blob (along B) that is electrically connected to sheaths,  $L_{\parallel}/R$  is the length of the field line weighted by the normal curvature. More generally,  $L_{\parallel}$  in the theory includes an effective blob pressure-weighting that is not measured. These ambiguities plus the uncertainty of the separatrix location ( $\pm 1$  to 1.5 cm) preclude an accurate evaluation of  $q$  for each blob. Instead, we consider the minimum velocity in the sheath connected regime, obtained by estimating  $q \approx 1$ ,

$$v_{\min} = c_s f_b \frac{\rho_s^2}{a_b^2} = 1.4 \times 10^{10} \frac{f_b T_e^{3/2}}{a_b^2 B^2} \quad (10)$$

This  $q = 1$  bound is based on the assumption that the ballooning structure of the turbulence will create blobs with a *minimum* parallel pressure length of order  $R$ , consistent with the *local* outboard-midplane edge magnetic rotational transform ( $\sim 1$ ) for NSTX geometry. Of course, it is also possible that turbulence may eject some blobs with longer filaments that reach right up to the X-point where field lines become very long. Also, as blobs propagate into the SOL, sonic flow is expected to lengthen the blob parallel scale length until it reaches the sheaths. Electrical connection of a blob to the sheaths can also be facilitated by the background plasma on which the blob propagates. For all these reasons, Eq. (10) represent a lower bound that is expected to be exceeded in many cases.

In Fig. 5 we show the observed radial blob velocity vs.  $v_{\min}$ . Most of the data lies in the upper triangle, indicating that the theoretical minimum is obeyed by the dataset, i.e. that the first inequality of Eq. (4) is satisfied with  $q = 1$ . Details of the application of Eq. (10) (and the RB scaling to be considered subsequently) to the dataset are given in an Appendix.

A more stringent test, not possible here, would take the proper  $q(r)$  into account. Alternatively, we define  $q_{\text{eff}} = v_{\text{observed}}/v_{\text{min}}$  and plot the resulting radial dependence  $q_{\text{eff}}(r)$  in Fig. 6. In effect, this figure represents all the dependencies of  $v_r$  not taken into account by Eq. (10). From the figure we see that, although there is significant scatter,  $q_{\text{eff}}$  displays the qualitative features expected of  $q(r)$  from the magnetic geometry, viz. large as one approaches the separatrix, and decaying into the far SOL. There are many plausible candidates for the residual scatter. These include analysis errors, parallel blob structure, different background plasma parameters at the midplane and at the divertor plates where the blob sheaths form, and blob spin<sup>44</sup> which, while difficult to observe with the GPI diagnostic, can theoretically affect the speed. The internal “radial” blob electric field required for spin has been observed from conditionally averaged probe signals<sup>4</sup> on the DIII-D<sup>45</sup> tokamak.

Analogous to the minimum velocity provided by the sheath-connected regime, the resistive ballooning regime gives a theoretical maximum velocity for blob convection,

$$v_{\text{max}} = c_s f_b \left( \frac{a_b}{R} \right)^{1/2} \sim 6.9 \times 10^5 \frac{a_b^{1/2} f_b T_e^{1/2}}{R^{1/2}} \quad (11)$$

The observed velocity  $v_r$  is plotted against  $v_{\text{max}}$  in Fig. 7. The data lie fully in the lower triangle, indicating the observed  $v_r$  is bounded by the theoretical maximum. This shows that the second inequality of Eq. (4) is satisfied. Indeed, as might be expected from Fig. 1, which shows this NSTX plasma to be quite far from the RB regime,  $v_r$  is well below  $v_{\text{max}}$ .

The preceding blob velocity scaling studies demonstrate the main new result of the paper, namely, the contact of experimental data with the theoretically predicted sheath-connected and resistive ballooning bounds described by Eq. (4). In addition, we have also used the dataset to examine the question of where blobs are born. For this analysis, we determined the first time-instance in which a blob could be identified by the

maxima-tracking algorithm. Figure 8 shows the density of these “young” blobs as solid circles. Under the convective ansatz, these blobs could have acquired their density only by interchange with the background profile. Thus, projecting the observed blob parameters onto the background profiles defines a blob birth zone. Examination of the normalized pressure gradient within the birth zone (see the lower panel) shows that blobs are born with a density (and temperature) characteristic of the region where the local logarithmic pressure gradient peaks. This is the region where pressure-gradient-driven curvature and drift instabilities maximize. Thus the data is consistent with blob generation by the turbulence arising from edge instabilities. These statements should not be confused with so called “fixed-gradient-driven turbulence” models in the theoretical literature. It is important to note that the edge pressure gradient arises *self-consistently* in the experiment, presumably by balancing the blob transport out of the birth zone with flux from the core (and/or ionization) that refuels that region. Additionally, large nonlinear perturbations ( $\delta n/n \sim 1$ ) can occur near the birth zone, so the concept of separating background profiles from blobs is necessarily heuristic in this region.

It has previously been observed that the blob density increases with the discharge density.<sup>4,5</sup> This observation can be understood in the context of the birth zone model. Assuming, for simplicity of argument, that the edge density and temperature profiles increase with discharge density while maintaining roughly constant shape, the radial location of the birth zone ( $\text{Max}[-\nabla \ln p]$ ) would remain unchanged. Thus the blobs which are born in this zone would convect a density proportional to the discharge density.

The analysis presented so far in this section involves many steps. To review, first, the raw camera emission data must be mapped to flux surfaces, for comparison to the TS data. The atomic physics function  $F(n_e, T_e)$  is then calculated and employed to construct the empirically determined  $n_0$  using the median frame method. Then the inverse mapping  $I \rightarrow (n_e, T_e(n_e))$  is constructed and applied to the time-dependent

movies. Blobs selection criteria are next applied. Tracking of these blobs allows their velocities to be measured and the blob properties database, including spatial scale size and peak  $n_e$ ,  $T_e$  to be constructed. Finally the database is analyzed using standard techniques and compared to the theoretical blob scalings. Many of these steps are difficult to automate. Consequently, we sought other, less labor intensive, procedures which could be applied to the GPI data for more shots.

For the remainder of this section, we describe a somewhat more automated analysis applied to four NSTX shots, which addresses several new questions. First, to what extent can the automated analysis reproduce or confirm the main trends of the preceding sheath-scaling studies? Second, how do blob properties (especially  $v_r$ ) vary with discharge conditions, and how large are any systematic variations compared with the statistical variations that occur within a given shot?

An automated blob identification and tracking algorithm was first employed to select “trackable” objects, i.e. local maxima appearing in successive (time) frames that were close enough spatially to be identified as the same object. Additional selection criteria were then applied. Candidate blobs were required to exceed an intensity threshold. The poloidal half-width-at-half-maximum determination of  $a_b$  on both sides were required to exist (eliminating objects near a frame boundary or too close to other turbulent structures) and to match within 20% (symmetry requirement). Candidate blobs were required to be trackable over at least five frames (20  $\mu$ s) to insure a coherent long-lived object for which a good  $v_r$  determination could be made. Then a database of the blob’s  $v_r$ ,  $a_b$ , intensity  $I$  and radial position  $r$ , was constructed for each shot.

The four shots employed for this analysis and corresponding parameters are summarized in Table I. These include the moderate density L-mode lower-single-null reference discharge for which the detailed analysis was performed, an otherwise similar discharge with almost a factor of two lower density, an H-mode discharge, and a double

null (DX) L-mode discharge with higher beam power. The table shows  $\bar{n}_e$  from an edge interferometer channel. All these shots employed the same He puff, magnetic field  $B_0 = 4.5$  kG ( $B_{\text{edge}} = 2.5$  kG), and plasma current  $I_p = 800$  kA. Visual inspection of the GPI movies for these shots reveals very different levels of blob activity, as indicated in the table: the reference discharge and the higher power DX case show a high level of turbulence and blob ejection while the H-mode and low density L-mode discharges are relatively quiescent.

Results for the normalized probability distribution functions (PDFs) of  $a_b$  and  $v_r$  are shown in Fig. 9. The typical half-width is  $a_b = 1.5 \pm 0.5$  cm. Note that this is  $a_b$  in the *poloidal* direction, the dimension most relevant to the basic blob propagation mechanism. Imaging data in 2D is key to obtaining this information. The blob radial velocity ranges from small negative values to about 1.5 km/s. The negative  $v_r$  occur for blobs near the birth zone which appear to be created and then trapped by turbulence and/or sheared flows. Statistics for the two more quiescent discharges are poor. For both  $a_b$  and  $v_r$  statistical variations within a shot exceed any systematic differences between shots. The main systematic difference is in the total number of blobs-frames (= blobs  $\times$  number of frames they are visible in): 53 and 45 for the reference and DX discharges respectively, 20 and 17 for the H-mode and low  $n_e$  discharges respectively. The independence of  $v_r$  on discharge density, seen here, has previously been reported in Ref. 5. It is important to note that in Fig. 9 the PDF for  $v_r$  includes blobs of all sizes, temperatures and radial locations, i.e. the main parameters that control the  $v_r$  scaling in Eq. (9) have all been mixed together.

To address the issue of correlations of  $v_r$  with these theoretical control parameters, Fig. 10 shows the mean and standard deviation of  $v_r$  binned by  $a_b$  and distance from the separatrix  $\Delta r$  for the four discharges. A weak trend towards faster blob velocities at small  $a_b$  and  $\Delta r$  is seen for the two most active (turbulent) discharges. The

total number of blobs available for binning in the two more quiescent discharges precludes any strong conclusions. While the results of Fig. 10 are not inconsistent with the more detailed scaling analysis presented earlier, the lack of a strong result indicates the difficulty of extracting systematic trends from these types of datasets.

The correlations between  $v_r$ ,  $a_b$  and  $\Delta r$  are illustrated another way in Fig. 11 for the two most turbulent discharges. High velocity blobs (the large filled circles) are clearly clustered at small  $a_b$  and  $\Delta r$ . The slowdown of blobs in the far SOL has also been reported by other authors.<sup>4,5,7</sup> The present observations can be understood in the context of the theoretical sheath scaling law, Eq. (9), which predicts lower velocities at larger  $\Delta r$  (i.e. smaller  $q$ ). Other mechanisms also give a slowing of  $v_r$  in the far SOL: (i) blob cooling implies lower velocities in the sheath-connected regime from the  $T_e$  scaling, (ii) blobs that are initially disconnected because the ejected plasma is localized to the outer midplane (i.e. the ballooning structure), can become connected as parallel sonic flow brings plasma into contact with the divertor plates,<sup>46</sup> (iii) sheath contact points and sheath plasma conditions vary radially. Note that these slowdown mechanisms in the far SOL are in competition with the radial decrease of the background profiles, which drives an increasing  $f_b(r)$  and hence an increasing  $v_r(r)$  in the near SOL.

## V. Discussion and conclusions

The main goal of our paper is to establish contact between experimental data and theory-based analytical scalings of the radial convection velocity of blobs. In order to undertake this comparison, and to maximize the overlay with assumptions in the analytical theories, we examined in detail the radial motion and properties of selected blobs, choosing bright, coherent, symmetric objects that were relatively isolated. The goal of this approach was to confirm (or refute) the basic mechanisms (and hence theoretical equations) underlying blob convection in a deterministic context, viz. blob

propagation, before proceeding with more complex tests which will require turbulence codes and sophisticated statistical comparisons.

The deterministic tests comparing the blob radial convection velocity  $v_r$  with theory-based scalings are highlighted in Figs. 5 and 7 which demonstrate adherence of the data to the theoretical minimum and maximum velocities given in Eq. (4), corresponding to the sheath-connected and resistive ballooning regimes. (See the main text for the caveat relating to the  $q$  portion of the sheath scaling.) Less sophisticated tests of certain features of the scaling, namely the gross dependence on blob size and connection length  $q$  (represented in the dataset by distance from the separatrix) were also carried out using automated blob tracking and selection algorithms. Such algorithms are being developed for application to the extremely large datasets (10,000 frames and more) being recorded by the next generation of cameras.

We find that detailed analysis of the data, taking into account simultaneous correlations of  $v_r$  with blob size, temperature (in general also density, except this does not appear in the sheath-connected and resistive ballooning regimes) and radial position  $r$  are necessary to extract scaling information. When these control parameters are mixed, as in Fig. 9, we find that the statistical variations of  $v_r$  within a shot are large, and for the cases examined, completely swamp any shot-to-shot variations due to different discharge conditions. The most significant and obvious quantity that varies as discharge conditions vary is simply the number of blobs produced.

The implications of this observation are two-fold. To understand the underlying physics of blob formation from turbulence, simultaneous measurements of the key parameters (at a minimum  $v_r$ ,  $a_b$ ,  $r$ ,  $T_e$  and  $n_e$ ) appears to be required. On the other hand, for some considerations, the large turbulence-induced statistical variations of blob properties within a discharge suggests the notion of approximate universality<sup>47</sup> among at

least certain classes of discharges with varying conditions (i.e. because of the masking of smaller systematic variations by turbulence-induced statistics).

More generally, the work presented here addresses the broad question of whether we can understand the radial convection of individual blobs with known properties ( $a_b$ ,  $n_e$ ,  $T_e$ ). Our conclusion is affirmative in the sense of being able to bound the observed velocity both above and below by simple first principles theoretical estimates. The fact we find bounds, rather than absolute scalings, is probably indicative of a hidden variable outside the scope of the present model and dataset. Possible candidates are the parallel structure of the blob, blob spin, and the background plasma properties at the divertor sheaths.

The theoretical bounds on blob  $v_r$  verified here for NSTX can also be applied to other experiments. We first consider the blob data of Grulke et al.<sup>6</sup> on Alcator C-Mod, where the dipole potential structure of the blob underlying the theory of Sec II was explicitly verified. From Eq. (4) we expect  $v_r$  to be in the range  $v_* / \hat{a}^2 < v_r < v_* \hat{a}^{1/2}$ . For C-Mod, Fig. 1 shows that  $\hat{a} \sim 3$  ( $a_b \sim 0.5$  cm,  $a_* \sim 0.17$  cm) hence we estimate, from Eq. (3),  $v_* / c_s \sim (a_* / R)^{1/2} \sim 0.05$  (using  $R = 88$  cm). Thus the expected velocity bound is  $0.6\% c_s < v_r < 8.6\% c_s$ . However these C-Mod parameters place the blob regime much closer to the sheath-connected lower bound than the resistive ballooning upper bound (Fig. 1). The mean  $v_r$  measured in Ref. 6 is  $\langle v_r \rangle = 500$  m/s  $\sim 1\% c_s$ , consistent with the preceding estimates. Other aspects of the present paper are also consistent with Ref. .6, in particular, our PDF's of radial velocity in Fig. 9 have a similar character to those seen on C-Mod, i.e. broad maxima and a small number of negative  $v_r$  (inward propagating) blobs. A tendency for larger  $v_r$  closer to the separatrix was noted in both experiments.

Turning to the DIII-D experiments reported by Rudakov et al.<sup>48</sup> and Boedo et al.,<sup>4</sup> nominal blob parameter are  $T_e = 20 - 80$  eV,  $a_b = 1 - 2$  cm,  $q = 10$ ,  $R = 175$  cm,  $B = 20$  kG, from which follows:  $v_* \sim 2 - 4$  km/s,  $\hat{a} \sim 1 - 3$ , and theoretical velocity bounds

in the range  $200 \text{ m/s} < v_r < 6000 \text{ m/s}$ . These compare well with measured velocities of order  $300 \text{ m/s}$  (near the wall) to as large as  $2500 \text{ m/s}$  near the separatrix.

In addition to exploring the velocity of blobs, a second topic of interest is that of understanding what properties ( $a_b$ ,  $n_e$ ,  $T_e$ , ...) the blobs are created with and why. The analysis of Fig. 8 suggests the concept of a blob birth zone related to the localization of the underlying edge instabilities (i.e.  $\nabla \ln p$ ). It was shown that blobs are created with a density and temperature characteristic of the background plasma in this birth zone. This conclusion is supported by earlier work on DIII-D which showed that blobs have characteristics proportional to those of the pedestal.<sup>4,48</sup> Remaining for future work is an understanding of what controls the distribution of blob sizes and the rate at which they are produced.

Ultimately, for the assessment of wall and divertor interactions, an estimate of the particle (and thermal) flux  $\Gamma$  is required, or equivalently, (balancing flux against classical parallel losses) the SOL width.<sup>49</sup> In the blob paradigm we have  $\Gamma \sim (n_e v_r)_{\text{blob}} f_p$ , where the blob “packing fraction” accounts for temporal and spatial intermittency. The velocity scaling studied here together with birth parameter information on  $n_e$  (and  $T_e$ ) yields part of the net radial flux scaling. Additional work on intermittency statistics ( $f_p$ ) is also required. Some recent blob-based theoretical and computational work on the question of the scaling of the intermittent particle flux with connection length has been reported.<sup>50,51</sup> In these papers, estimates of the blob velocity are combined with assumptions concerning the blob scale size, role of diffusion and the parallel losses, to obtain the scaling of the SOL width. In Ref. 50 the RB regime for blob propagation ( $v_r$ ) is effectively assumed, while Ref. 51 treats the sheath-connected (C) regime. The present work and Ref. 36 complement these interesting approaches by seeking a more complete understanding of the role of regimes on  $v_r$  itself.

Further investigations of the blob birth parameters, intermittency statistics and flux scaling are expected to be fascinating from the perspective of fundamental physics, and of considerable importance for making first principles predictions of SOL characteristics in fusion-relevant magnetic confinement devices.

## Acknowledgments

The authors wish to thank the NSTX team for their support of the GPI experiments. Discussions with D. Russell, R. Maingi and T. Munsat are gratefully acknowledged. This work was supported by U.S. Department of Energy (DOE) under grant DE-FG02-02ER54678; however, such support does not constitute an endorsement by the DOE of the views expressed herein.

## Appendix: Application of scaling laws to the dataset

When blobs propagate on a background plasma (as opposed to free propagation in a vacuum) their velocity is generally slowed, and the dependencies on plasma parameters such as  $n_e$  and  $T_e$  are complicated by different blob and background values. In the main text, these effects are absorbed into the factor  $f_b$ ; here, we present a more detailed examination of the scalings and how they are applied to the data.

For each plasma parameter,  $Q = n_e, T_e$ , and corresponding derived quantities such as  $c_s$  and  $\rho_s$ , we define blob, background, and average quantities denoted respectively  $Q_b, Q_0$  and  $Q_{avg}$ . Here  $Q_b$  denotes the maximum value at the center of the blob, and  $Q_{avg} = 0.5 (Q_0 + Q_b)$ .

Blob convection is driven by the pressure-gradient weighted curvature term in the vorticity equation, thus<sup>20</sup> we expect  $v_r$  to be proportional to  $\delta p = p_b - p_0$ . For the sheath connected limit (balancing curvature-drift current with sheath end-loss current)<sup>16,17</sup> we deduce that

$$v_{r,C} = 0.5 \frac{q c_{s,avg}}{n_{e,avg} a_b} \left( n_{e,b} \rho_{s,b}^2 - n_{e,0} \rho_{s,0}^2 \right) \quad (\text{A1})$$

Here,  $a_b$  is the half-width of the blob in the poloidal direction. Note that in the limit of an isolated, thermalized ( $T_{e0} = T_{eb}$ ), Gaussian profile blob propagating in a vacuum, Eq. (A1) (with the factor of 0.5, and the preceding definitions for ‘‘avg’’) reduces to the analytic result.<sup>16,17</sup> A similar treatment of the background and blob parameters for the sheath-connected regime has been employed by Endler<sup>52</sup> to describe edge-localized-mode (ELM) convection in the SOL.

In the fully disconnected resistive ballooning limit (balancing curvature-drift current with ion polarization-drift current, i.e. inertia)<sup>32</sup> we obtain

$$v_{r,RB} = \left( \frac{a_b}{n_{e,avg} R} \left( n_{e,b} c_{s,b}^2 - n_{e,0} c_{s,0}^2 \right) \right)^{1/2} \quad (\text{A2})$$

It may be verified that Eqs. (A1) and (A2) correspond to the lower and upper bounds given in Eq. (4) of the main text, by employing Eqs. (2) and (3) to eliminate  $\hat{a}$  and  $v_*$ . In particular, Eqs. (A1) and (A2) are consistent with the scalings of  $\hat{a}$  and  $v_*$  with  $B, R, L_{||}$  and  $T_e$  asserted in the main text. In general  $v_r$  depends on the collisionality parameter  $\Lambda$ ;<sup>53</sup> however, the lower and upper velocity *bounds* are independent of  $\Lambda$ . Further details of these scaling arguments are given in Ref. 36.

## References

- <sup>1</sup> A. J. Wootton, B. A. Carreras, H. Matsumoto, *et al.*, Phys. Fluids B **2**, 2879 (1990).
- <sup>2</sup> M. Endler, H. Niedermeyer, L. Giannone, *et al.*, Nucl. Fusion **35**, 1307 (1995).
- <sup>3</sup> S.J. Zweben and R.W. Gould, Nucl. Fusion **25**, 171 (1985).
- <sup>4</sup> J. A. Boedo, D. L. Rudakov, R. A. Moyer, *et al.*, Phys. Plasmas **10**, 1670 (2003).
- <sup>5</sup> D.L. Rudakov, J.A. Boedo, R.A. Moyer, *et al.*, Nucl. Fusion **45**, 1589 (2005).
- <sup>6</sup> O. Grulke, J.L. Terry, B. LaBombard, and S.J. Zweben, Phys. Plasmas **13**, 012306 (2006).
- <sup>7</sup> G. S. Kirnev, V. P. Budaev, S. A. Grashin, E. V. Gerasimov, and L. N. Khimchenko, Plasma Phys. Control. Fusion **46**, 621 (2004).
- <sup>8</sup> G. Y. Antar, G. Counsell, J.-W. Ahn, Y. Yang, M. Price, A. Tabasso and A. Kirk, Phys. Plasmas **12**, 032506 (2005).
- <sup>9</sup> P. Devynck, P. Ghendrih, Y. Sarazin, Phys. Plasmas **12**, 050702 (2005).
- <sup>10</sup> Y.H. Xu, S. Jachmich, R.R. Weynants and the TEXTOR team, Plasma Phys. Control. Fusion **47**, 1841 (2005).
- <sup>11</sup> T. A. Carter, Phys. Plasmas **13**, 010701 (2006).
- <sup>12</sup> Å. Fredriksen, C. Riccardi, L. Cartegni and H. Pécseli, Plasma Phys. Control. Fusion **45**, 721 (2003).
- <sup>13</sup> M. Spolaore, V. Antoni, E. Spada, H. Bergsaker, R. Cavazzana, J. R. Drake, E. Martines, G. Regnoli, G. Serianni, and N. Vianello, Phys. Rev. Lett. **93**, 215003 (2004).
- <sup>14</sup> S. J. Zweben, R. J. Maqueda, D. P. Stotler, *et al.*, Nucl. Fusion **44**, 134 (2004).
- <sup>15</sup> J. L. Terry, S. J. Zweben, K. Hallatschek, *et al.*, Phys. Plasmas **10**, 1739 (2003).
- <sup>16</sup> S. I. Krasheninnikov, Phys. Lett. A **283**, 368 (2001).
- <sup>17</sup> D. A. D'Ippolito, J. R. Myra, and S. I. Krasheninnikov, Phys. Plasmas **9**, 222 (2002).

- <sup>18</sup> N. Bian, S. Benkadda, J.-V. Paulsen, and O. E. Garcia, *Phys. Plasmas* **10**, 671 (2003).
- <sup>19</sup> G. Q. Yu and S. I. Krasheninnikov, *Phys. Plasmas* **10**, 4413 (2003).
- <sup>20</sup> D.A. D'Ippolito, J.R. Myra, S.I. Krasheninnikov, G.Q. Yu and A. Yu. Pigarov, *Contrib. Plasma Phys.* **44**, 205 (2004).
- <sup>21</sup> N. Bisai, A. Das, S. Deshpande, *et al.*, *Phys. Plasmas* **12**, 102515 (2005).
- <sup>22</sup> Y. Sarazin and Ph. Ghendrih, *Phys. Plasmas* **5**, 4214 (1998).
- <sup>23</sup> Ph. Ghendrih, Y. Sarazin, G. Attuel, *et al.*, *Nucl. Fusion* **43**, 1013 (2003).
- <sup>24</sup> S. Benkadda, P. Beyer, N. Bian, *et al.*, *Nucl. Fusion* **41**, 995 (2001).
- <sup>25</sup> X. Q. Xu, W. M. Nevins, R. H. Cohen, *et al.*, *New J. Phys.* **4**, 53 (2002).
- <sup>26</sup> D. A. Russell, D. A. D'Ippolito, J. R. Myra, W. M. Nevins, and X. Q. Xu, *Phys. Rev. Lett.* **93**, 265001 (2004).
- <sup>27</sup> B.N. Rogers, J.F. Drake and A. Zeiler, *Phys. Rev. Lett.* **81**, 4396 (1998).
- <sup>28</sup> B.D. Scott, *Phys. Plasmas* **12**, 062314 (2005).
- <sup>29</sup> P. Beyer P, S. Benkadda, G. Fuhr-Chaudier *et al.*, *Phys. Rev. Lett.* **94**, 105001 (2005).
- <sup>30</sup> B.A. Carreras, *J. Nucl. Mater.* **337-339**, 315 (2005).
- <sup>31</sup> V. Naulin, "Turbulent transport and the plasma edge" submitted to *J. Nucl. Mater.* (2006).
- <sup>32</sup> J.R. Myra and D. A. D'Ippolito, *Phys. Plasmas* **12**, 092511 (2005).
- <sup>33</sup> S. I. Krasheninnikov, A. I. Smolyakov, G. Yu, and T. K. Soboleva, *Czech. J. Phys.* **55**, 307 (2005).
- <sup>34</sup> R. J. Maqueda, G. A. Wurden, D. P. Stotler, *et al.*, *Rev. Sci. Instrum.* **74**, 2020 (2003).
- <sup>35</sup> M. Ono, M.G. Bell, R.E. Bell *et al.*, *Plasma Phys. Control. Fusion* **45**, A335 (2003).
- <sup>36</sup> J.R. Myra, D. A. Russell and D.A. D'Ippolito, "Collisionality and magnetic geometry effects on edge turbulent transport: I. A two-region model with application to blobs", submitted to *Phys. Plasmas* (2006).
- <sup>37</sup> D.D. Ryutov and R.H. Cohen, *Contrib. Plasma Phys.* **44**, 168 (2004).

- <sup>38</sup> S.I. Krasheninnikov, D.D. Ryutov, and G.Q. Yu, *J. Plasma Fusion Res.* **6**, 139 (2005).
- <sup>39</sup> E. Marmor, B. Bai, R.L. Boivin *et al.*, *Nucl. Fusion* **43**, 1610 (2003).
- <sup>40</sup> O.E. Garcia, N.H. Bian, V. Naulin, A.H. Nielsen and J.J. Rasmussen, *Phys. Plasmas* **12**, 090701 (2005).
- <sup>41</sup> T. Fujimoto, *J. Quant. Spectrosc. Radiat. Transfer* **21**, 439 (1979).
- <sup>42</sup> M. Goto, *J. Quant. Spectrosc. Radiat. Transfer* **76**, 331 (2003).
- <sup>43</sup> D. P. Stotler, J. Boedo, B. LeBlanc, R. J. Maqueda, and S. J. Zweben, “Details of neutral transport in gas puff imaging experiments” submitted to *J. Nucl. Mater.* (2006).
- <sup>44</sup> J. R. Myra, D. A. D’Ippolito, S. I. Krasheninnikov, and G. Q. Yu, *Phys. Plasmas* **11**, 4267 (2004).
- <sup>45</sup> J. L. Luxon, *Nucl. Fusion* **42**, 614 (2002).
- <sup>46</sup> R.H. Cohen and D. D. Ryutov, *Bull. Am. Phys. Soc.* **50**, 83 (2005), paper CP1-43.
- <sup>47</sup> G. Y. Antar, G. Counsell, Y. Yu, B. LaBombard, and P. Devynck, *Phys. Plasmas* **10**, 419 (2003).
- <sup>48</sup> D. L. Rudakov, J. A. Boedo, R. A. Moyer, *et al.*, *Plasma Phys. Control. Fusion* **44**, 717 (2002).
- <sup>49</sup> J.W. Connor, G.F. Counsell, S.K. Erents, *et al.*, *Nucl. Fusion* **39**, 169 (1999).
- <sup>50</sup> Ph. Ghendrih, P. Kaw, Y. Sarazin, *et al.*, Proceedings of the 20th IAEA. Fusion Energy Conference, Villamoura, Portugal, 2004 (International Atomic Energy Agency, Vienna, 2005), paper TH/1-3Ra.
- <sup>51</sup> A.Y. Aydemir, *Phys. Plasmas* **12**, 062503 (2005).
- <sup>52</sup> M. Endler, I. García-Cortés, C. Hidalgo, G. F. Matthews, ASDEX Team and JET Team, *Plasma Phys. Control. Fusion* **47**, 219 (2005).
- <sup>53</sup> D.A. D’Ippolito and J.R. Myra, *Phys. Plasmas* **13**, 062503 (2006).

## Tables

Table 1. Discharge parameters for the analysis results presented in Figs. 9 - 11.

shot #	conf. mode	edge $\bar{n}_e$ ( $10^{13} \text{ cm}^{-3}$ )	$P_{\text{nbi}}$ (MW)	blob activity
112825	L	4.0	0.8	turbulent
112814	L	2.5	0.8	quiescent
112842	H	2.0	0.8	quiescent
112844	L (DX)	3.0	1.7	turbulent

## Figure captions

1. (color online) Regime diagram for blob propagation in the space of dimensionless collisionality  $\Lambda$ , and blob scale size  $\hat{a}$ . The resistive ballooning (RB), resistive X-point (RX), and sheath connected interchange (C) regimes are indicated, as well as the nominal location of typical NSTX and Alcator C-Mod edge plasmas.
2. (color online) Zoomed-in portion of a sample GPI frame showing an elongated turbulent pattern (at left) just outside the separatrix, and a blob that has been ejected into the far SOL (at right). The separatrix location is uncertain to perhaps 1 – 2 cm. The rainbow color palette shows high intensity ( $n_e$  and  $T_e$ ) in red (dark gray), low in blue (light gray).
3. (color online) Radial profiles of the background  $n_e$  (solid),  $T_e$  (dashed), and the empirically inferred  $n_0$  (dotted) for shot #112825. The  $n_0$  profile is for a cut through the center of the GPI image and  $\Delta r$  is the distance from a nominal separatrix location. Note that  $n_0$  is the diagnostic gas (He) not the working gas (D).
4. (color online) Observed radial velocity of five individual blob tracks (indicated by different colors/shades) vs. radial distance  $\Delta r$  from a nominal separatrix location. Typical error bars are shown for one point. There is little apparent order in the dataset.
5. (color online) Observed radial blob velocity vs. the minimum sheath-connected velocity. The dashed line is  $v_{\text{observed}} = v_{\text{min}}$ . Most of the data lies in the upper triangle, indicating that the observed  $v_r$  is bounded by the theoretical minimum. The large error in the theoretical  $v_{\text{min}}$  is dominated by uncertainties in  $a_b$  and the sensitive  $1/a_b^2$  scaling.
6. (color online) Variation of  $q_{\text{eff}} \equiv L_{\parallel\text{eff}}/R$  with radial distance from the separatrix. With significant scatter,  $q_{\text{eff}}$  displays the qualitative features expected from the

magnetic geometry, viz. larger as one approaches the separatrix, and decaying into the far SOL.

7. (color online) Observed radial blob velocity vs. the maximum (resistive ballooning) velocity, with typical error bars. The dashed line is  $v_{\text{observed}} = v_{\text{max}}$ . The data lies fully in the lower triangle, indicating the observed  $v_r$  is bounded by the theoretical maximum.
8. (color online) Density and normalized pressure gradient vs. distance from the separatrix. Dots in the upper panel correspond to the start of individual blobs tracks at the point of first detection. The solid curves are smoothed background profiles obtained from the Thomson scattering data.
9. (color online) Normalized PDFs of a) the blob size  $a_b$ , and b) the radial velocity  $v_r$  for 4 discharges: solid (red) #112825 reference discharge, dashed (blue) #112814 low  $n_e$ , dotted (green) #112842 H-mode, and long dashed (grey) #112844 DX.
10. (color online) Radial blob velocity for four discharges binned by blob size  $a_b$  and distance from the separatrix,  $\Delta r$ . The mean and standard deviation for each bin are shown, when more than 2 blobs are in a bin. The symbols S and L along the x-axis indicate whether the bins contain “small” or “large” values of  $a_b$  and  $\Delta r$ . Bin boundaries were determined to distribute the blobs in comparable numbers over bins, as far as possible.
11. (color online) Correlation of  $v_r$  with  $a_b$  and  $\Delta r$  for the two most turbulent discharges. High velocity blobs ( $v_r$  exceeding a threshold value) are shown with large symbols, low velocity blobs with small symbols. Data points are color/shape-coded by discharge.

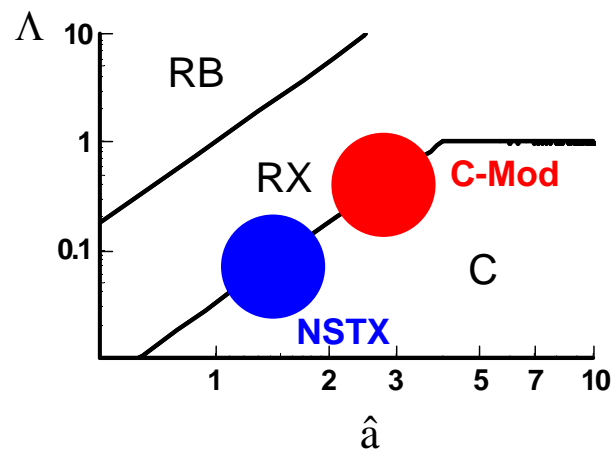


Fig. 1

Regime diagram for blob propagation in the space of dimensionless collisionality  $\Delta$ , and blob scale size  $\hat{a}$ . The resistive ballooning (RB), resistive X-point (RX), and sheath connected interchange (C) regimes are indicated, as well as the nominal location of typical NSTX and Alcator C-Mod edge plasmas.

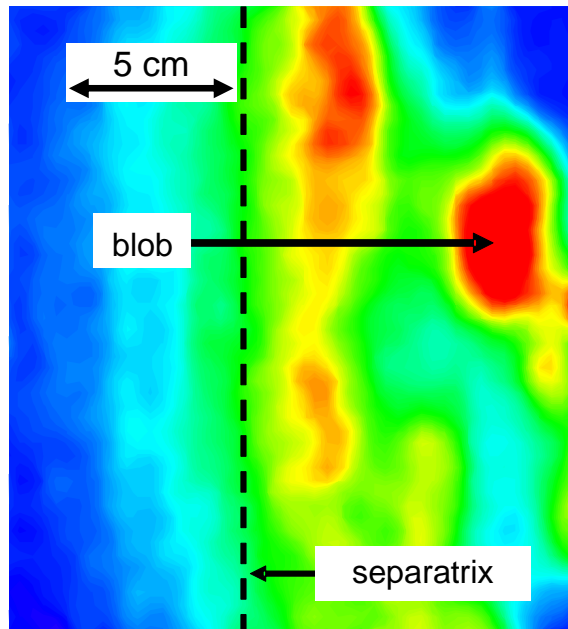


Fig. 2

Zoomed-in portion of a sample GPI frame showing an elongated turbulent pattern (at left) just outside the separatrix, and a blob that has been ejected into the far SOL (at right) . The separatrix location is uncertain to perhaps 1 – 2 cm. The rainbow color palette shows high intensity ( $n_e$  and  $T_e$ ) in red (dark grey), low in blue (light gray).

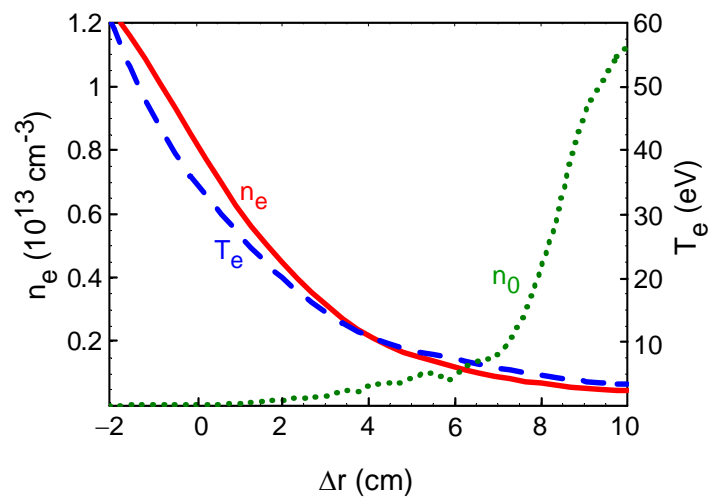


Fig. 3

Radial profiles of the background  $n_e$  (solid),  $T_e$  (dashed), and the empirically inferred  $n_0$  (dotted) for shot #112825. The  $n_0$  profile is for a cut through the center of the GPI image and  $\Delta r$  is the distance from a nominal separatrix location.

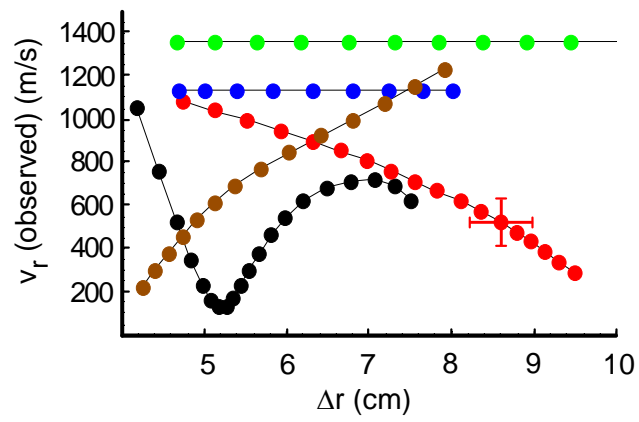


Fig. 4

Observed radial velocity of five individual blob tracks (indicated by different colors/shades) vs. radial distance  $\Delta r$  from a nominal separatrix location. Typical error bars are shown for one point. There is little apparent order in the dataset.

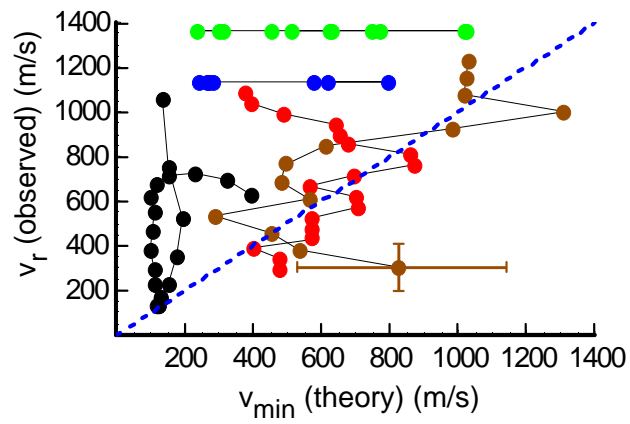


Fig. 5

Observed radial blob velocity vs. the minimum sheath-connected velocity. The dashed line is  $v_{\text{observed}} = v_{\text{min}}$ . Most of the data lies in the upper triangle, indicating that the observed  $v_r$  is bounded by the theoretical minimum. The large error in the theoretical  $v_{\text{min}}$  is dominated by uncertainties in  $a_b$  and the sensitive  $1/a_b^2$  scaling.

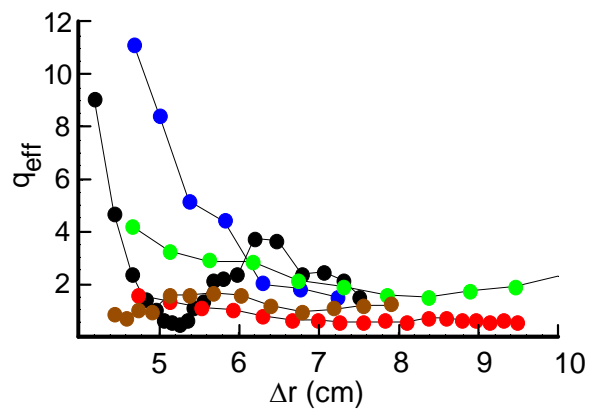


Fig. 6

Variation of  $q_{\text{eff}} = L_{\parallel\text{eff}}/R$  with radial distance from the separatrix. With significant scatter,  $q_{\text{eff}}$  displays the qualitative features expected from the magnetic geometry, viz. larger as one approaches the separatrix, and decaying into the far SOL.

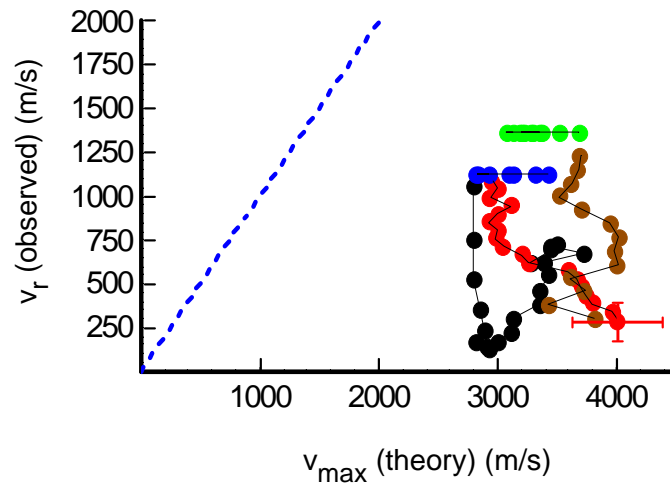


Fig. 7

Observed radial blob velocity vs. the maximum (resistive ballooning) velocity, with typical error bars. The dashed line is  $v_{\text{observed}} = v_{\text{max}}$ . The data lies fully in the lower triangle, indicating the observed  $v_r$  is bounded by the theoretical maximum.

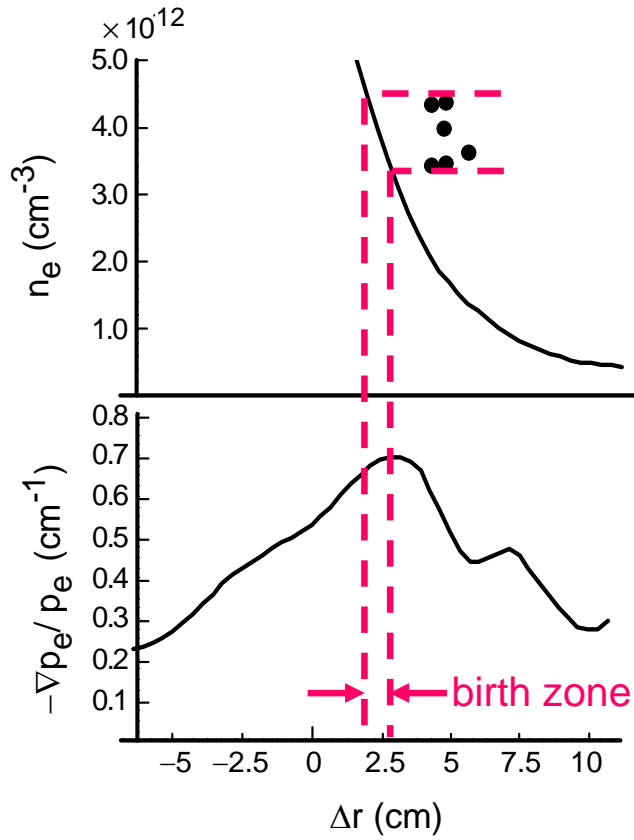


Fig. 8

Density and normalized pressure gradient vs. distance from the separatrix. Dots in the upper panel correspond to the start of individual blobs tracks at the point of first detection. The solid curves are smoothed background profiles obtained from combining TS and probe data.

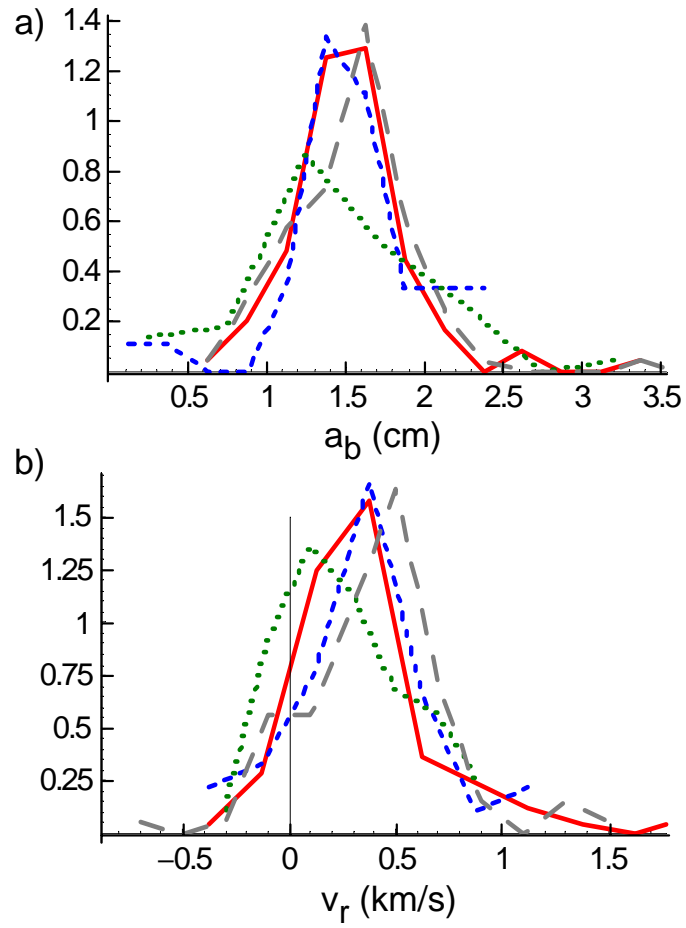


Fig. 9

Normalized PDFs of a) the blob size  $a_b$ , and b) the radial velocity  $v_r$  for 4 discharges: solid (red) #112825 reference discharge, dashed (blue) #112814 low  $n_e$ , dotted (green) #112842 H-mode, and long dashed (grey) #112844 DX.

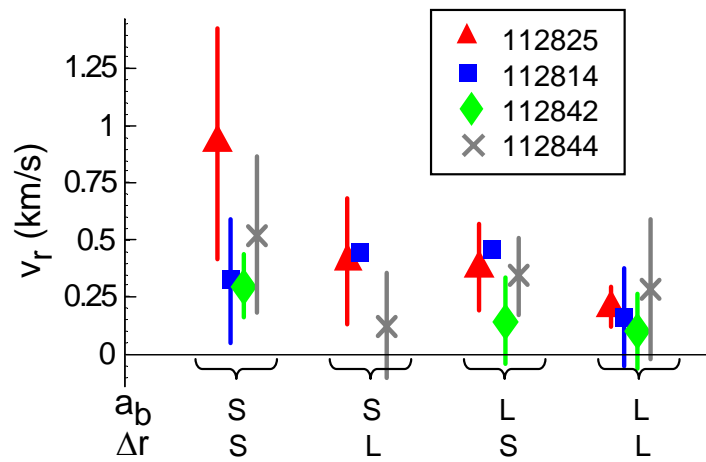


Fig. 10

Radial blob velocity for four discharges binned by blob size  $a_b$  and distance from the separatrix,  $\Delta r$ . The mean and standard deviation for each bin are shown, when more than 2 blobs are in a bin. The symbols S and L along the x-axis indicate whether the bins contain “small” or “large” values of  $a_b$  and  $\Delta r$ . Bin boundaries were determined to distribute the blobs in comparable numbers over bins, as far as possible.

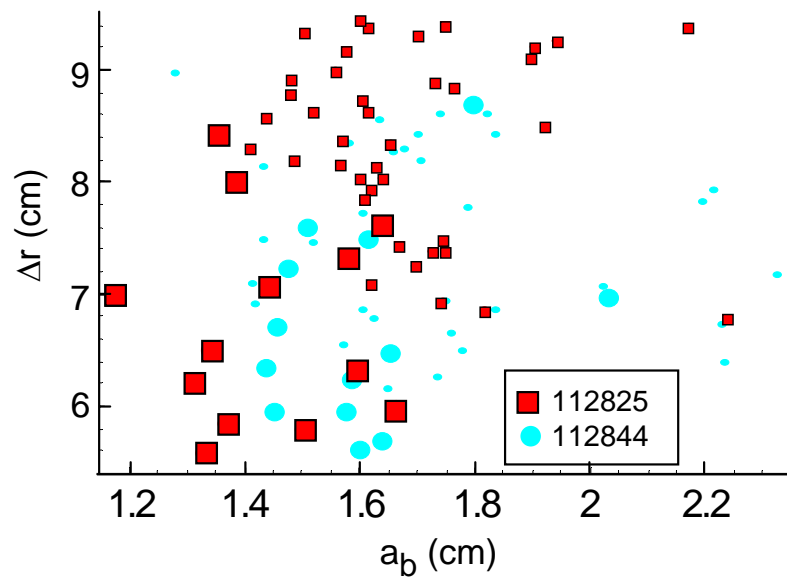


Fig. 11

Correlation of  $v_r$  with  $a_b$  and  $\Delta r$  for the two most turbulent discharges. High velocity blobs ( $v_r$  exceeding a threshold value) are shown with large symbols, low velocity blobs with small symbols. Data points are color/shape-coded by discharge.